PHYSICAL REVIEW C **77**, 035804 (2008)

Fission cycling in a supernova *r* process

J. Beun* and G. C. McLaughlin
Department of Physics, North Carolina State University, Raleigh, North Carolina 27595-8202, USA

R. Surman
Department of Physics, Union College, Schenectady, New York 12308, USA

W. R. Hix
Physics Division, Oak Ridge National Laboratory, Oak Ridge, Tennessee 37831-6374, USA
(Received 9 October 2007; published 13 March 2008)

Recent halo star abundance observations exhibit an important feature of consequence to the *r* process: the presence of a main *r* process between the second and third peaks that is consistent among halo stars. We explore fission cycling and steady β flow as the driving mechanisms behind this feature. The presence of fission cycling during the *r* process can account for nucleosynthesis yields between the second and third peaks, whereas the presence of steady β flow can account for consistent *r*-process patterns, robust under small variations in astrophysical conditions. We employ the neutrino-driven wind of the core-collapse supernova to examine fission cycling and steady β flow in the *r* process. As the traditional neutrino-driven wind model does not produce the required very neutron-rich conditions for these mechanisms, we examine changes to the neutrino physics necessary for fission cycling to occur in the neutrino-driven wind environment, and we explore under what conditions steady β flow is obtained.

DOI: 10.1103/PhysRevC.77.035804 PACS number(s): 26.30.−k, 14.60.Lm, 24.75.+i

I. INTRODUCTION

The production of neutron-capture elements early in the universe is recorded in the abundances of galactic halo stars. The two mechanisms responsible for generating most neutron-capture elements are the *r* process and the *s* process, with the *r* process generating about half of the nuclides with $A \gtrsim 100$ [1–3]. The observed *r*-process abundance distribution in metal-poor halo stars diverges above and below $Z \approx 58$ into two distinct patterns [4–15]. These patterns are defined by their consistency with the solar and halo star *r*-process abundances. The low *r*-process pattern ($Z \lesssim 58$) may result from the contributions of a light element production process (LEPP); see, e.g., Ref. [16] for additional discussion. The high abundance ($58 \lesssim Z \lesssim 76$) pattern, known as the main *r* process, is very consistent among both the available halo star data and the solar system *r*-process abundances [17,18]. We suggest the existence of a main *r* process implies that a robust mechanism is producing elements from the second ($A \approx 130$) through the third ($A \approx 195$) *r*-process peak region [19,20].

Although there has been success in observing the abundance fingerprints of the *r* process, determining the astrophysical production site(s) remains an open question [21–26]. A promising candidate site for the *r* process is the neutrino-driven wind of the postbounce core-collapse supernova, as the amount of *r*-process material ejected can account for the galactic abundances [23,27]. Also, the frequency of the core-collapse supernova event is sufficiently rapid to produce *r*-process material early in the universe, in accordance with the *r*-process abundances observed in very metal-poor stars [28]. However, traditional models of the neutrino-driven wind do not quite yield an *r* process due to the low free neutron abundance at the *r*-process epoch [29,30].

The *r* process requires a neutron-to-seed ratio of $R \gtrsim 100$ for production of the heaviest, $A \approx 195$, peak [3]). Uncertainties in the wind model may be responsible for this shortcoming as R is related to both the entropy, S, and the dynamical timescale, τ, and both are sensitive to the the proto-neutron star physics (see, e.g., Ref. [31]); an increase of S and a decrease of τ both lead to a higher initial neutron-to-seed ratio, R [29]. These changes would likely require a compact and/or massive proto-neutron star [27,30,32–34]. Additional studies have looked to a prompt supernova explosion mechanism for producing the neutron-rich conditions necessary for the *r* process [35,36], although the physical realization of a prompt explosion scenario remains uncertain [37,38].

An avenue that has been suggested for generating a suitable neutron-to-seed ratio is a shocked wind solution. A supersonic wind expansion, reducing seed formation during the α-particle formation epoch, is followed by a deceleration at late times [30,39] that allows the remaining free neutrons to be fully reincorporated into the *r* process. Recent *r*-process models in this supersonic outflow scenario can reproduce the solar system abundances but require an artificially high neutron-to-proton ratio [40]. Alternate wind solutions generated solely by magnetic fields or acoustic waves, e.g., Refs. [41,42], also do not appear to produce a high-enough neutron-to-seed ratio for an *r* process. Given these difficulties, alternative sites remain viable candidates, including neutron star mergers [25] and γ ray bursts [43,44].

*jbbeun@unity.ncsu.edu

In the neutrino-driven wind environment, charged-current neutrino reactions on both nucleons and nuclei determine the neutron-to-seed ratio for the r process. The relevant neutrino interactions on nucleons are

$$\nu_e + \mathrm{n} \rightleftharpoons \mathrm{p} + e^-, \quad (1)$$

$$\bar{\nu}_e + \mathrm{p} \rightleftharpoons \mathrm{n} + e^+. \quad (2)$$

For example, when electron antineutrino capture creating neutrons, Eq. (1), is favored over electron neutrino capture creating protons, Eq. (2), a higher neutron-to-proton ratio results. These reactions are sensitive to the hardness of the electron neutrino and antineutrino spectra, which we parametrize by the effective electron neutrino and antineutrino temperature, T_{ν_e} and $T_{\bar{\nu}_e}$, the electron neutrino and antineutrino luminosity, L_{ν_e} and $L_{\bar{\nu}_e}$, and the distance from the center of the proto-neutron star. An analytic form of these neutrino-nucleon capture rates is found in Ref. [45]. Neutrino-nucleon reactions are responsible for the "alpha" effect, a critical detriment to the r process in the presence of a high electron neutrino flux during the α-particle formation epoch [45–47]. There have been several physical modifications proposed to reduce the efficacy of the "alpha" effect; for instance, a fast outflow wind [29] or active-sterile neutrino oscillations [48–50] lead to a successful r process. Both mechanisms reduce the capture of free neutrons by electron neutrinos during the α-particle formation epoch, allowing for a successful r process.

When classifying the neutron richness of the r process, we employ the electron fraction:

$$Y_e = \frac{N_p}{N_p + N_n}, \quad (3)$$

where N_n and N_p are the total neutron and proton number densities, including both free nucleons and those in nuclei. The neutron-to-proton ratio may be taken as N_n/N_p. Environments with a low electron fraction have the high free neutron densities necessary to drive the rapid capture of neutrons onto seed nuclei, generating increasingly heavier nuclides by atomic weight, A. During the r process, these nuclei capture neutrons, become increasingly β unstable, and undergo β decay to proceed to a larger atomic number, Z. After β decay, the nuclide can again capture neutrons and the cycle repeats. As the supply of free neutrons dwindles, the nuclides decay back to β stability. The union of rapid neutron capture and β decay results in an abundance pattern distinguished by large peak features at $A \approx 80, 130,$ and195, the first, second, and third peaks, respectively. These peaks correspond to the closed-shell nuclei with slow β-decay rates, creating "waiting points," causing material to accumulate at these points.

Abundances of the second and third r-process peaks, and the intermediate nuclei between them, are defined by the nuclear properties of the r process under conditions where both steady β flow and fission cycling persist [51]. Fission cycling occurs for sufficiently neutron-rich conditions where the r process extends to nuclides that can decay through fission channels. Fission impacts the r process by terminating the path near the transuranium region. This termination results in material returning to the $A \approx 130$ peak [52]. If neutron-rich conditions persist, these fission products effectively become new seed nuclei for the r process, facilitating steady β flow.

Once a sufficient supply of both neutrons and seed nuclei are available, steady β flow correlates the r-process abundances to their inverse β-decay rates; see, e.g., Ref. [53] for further discussion. The individual abundances in N along an isotopic chain are determined by $(n, \gamma) \rightleftarrows (\gamma, n)$ equilibrium. These correlated abundances span two or more of the closed-shell regions, and when occurring between the second, $A \approx 130$, and third, $A \approx 195$, r-process peaks are a set of isotopic chains between $58 \lesssim Z \lesssim 76$. The Z of the last chain is determined by fission. The first and last chains are linked as material leaving the last chain becomes the seed nuclides for the first chain through fission cycling. The rate change of the total abundance of an isotopic chain, $Y(Z)$, is the difference between material entering and exiting the chain by β decay,

$$\dot{Y}(Z) = \sum_A Y(Z-1, A)\lambda_\beta(Z-1, A) - \sum_A Y(Z)\lambda_\beta(Z, A). \quad (4)$$

Above, the individual abundances of an isotopic chain are $Y(Z, A)$, and the individual β-decay rates are $\lambda_\beta(Z, A)$. If both $(n, \gamma) \rightleftarrows (\gamma, n)$ equilibrium and repopulation of the seed nuclei persist, the flow of material between isotopic chains reaches a steady-state configuration and the abundances and β-decay rates of each isotopic chain are inversely related as:

$$\sum_A Y(Z, A)\lambda_\beta(Z, A) = \text{const.} \quad (5)$$

This is known as the steady β-flow condition.

Here we examine fission cycling and steady β-flow mechanisms and discuss their impact on the r process in the neutrino-driven wind. We also explore changes to the neutrino physics, independent of a physical generator, that lead to environments where fission cycling and steady β-flow mechanisms are present in the neutrino-driven wind. In Sec. II, we describe the details of our calculation in the neutrino-driven wind. In Sec. III we describe how fission cycling influences the r process. Section IV describes how steady β flow leads to a robust r-process pattern. In Sec. V we detail how the neutrino spectrum influences the r-process environment. In Sec. VI, we summarize the results.

II. DESCRIPTION OF NUCLEOSYNTHESIS MODELING

The neutrino-driven wind forms several seconds postcore bounce in the core-collapse supernova environment, and a one-dimensional wind model is often employed to describe the abundance composition of the isotropic outflow [23,54]. Two-dimensional wind models have been employed previously; however, these calculations do not self-consistently account for neutrino interactions, necessitating the use of an artificial Y_e [55]. Here we follow the same wind parametrization as in Ref. [50]. Unless otherwise noted, our calculations use an entropy per baryon of $s/k = 100$, an outflow time scale of

$\tau = 0.3$ s, an initial density of $\rho_o \approx 1.7 \times 10^8$ g/cm^3, and an initial radius of $r_7 \approx 0.1$, in units of 10^7 cm.

We track the abundance composition of a mass element, following ejection from the proton-neutron star, using three coupled reaction networks. The element is initially in nuclear statistical equilibrium (NSE), and we follow it using a NSE network [48] until α particles begin to form, $T_9 \approx 10$, where T_9 is in units of 10^9 K. Next, we track the mass element throughout α-particle formation with an intermediate network calculation [56] that includes strong and electromagnetic rates tabulated by Ref. [57]. We have added electron, positron, neutrino, and antineutrino capture rates from Ref. [58] to both networks. As material reaches the r-process epoch, $T_9 \approx 2.5$, we use an r-process network [59,60] that handles the relevant reactions of β-decay, β-delayed neutron emission, neutron capture, and photodisintegration, and we include charged-current neutrino interactions. We use β-decay rates and neutron separations from Ref. [61], neutron capture rates from Ref. [57], and neutrino capture rates from Ref. [58]. A complete description of the network calculation can be found in Ref. [50].

III. FISSION CYCLING

Fission decay joins β decay, neutron capture, and photodissociation as a primary reaction channel for r-process nuclides near the transuranium region, as previously mentioned. Nuclei that undergo fission provide a termination point for the r process by preventing the production of heavier nuclides past this region. After the nuclide undergoes fission, it fragments into smaller nuclides that rejoin the r process in the $A \approx 130$ region. This leads to fission cycling, with the fission daughter products acting as seed nuclei for the r process.

A knowledge of both the location of fission and the resultant distribution of fission fragments are necessary for detailed calculations of the r process in very neutron-rich environments. Treatments of fission in the r process [62–65] have been limited to largely phenomenological methods because there are few measurements of the fission properties for neutron-rich heavy nuclides. This current study is concerned with the general effects of fission on the r process. We employ β-delayed fission probabilities from Ref. [66] that are relevant to our mass model and astrophysical conditions. We indirectly include the effects of neutron-induced fission, as no complete and consistent set of neutron-induced rates is available, by employing a spontaneous fission region for $A \gtrsim 270$, where all of the nuclides instantaneously fission, following previous treatments described in Ref. [67]. We implement fission by depopulating the parent fission nuclide into its appropriate daughter nuclides at the end of each time step in our network code. The effects of neutrino-induced fission are small and are not included [68,69]. We employ phenomenological fission distributions, following previous studies described in Ref. [67], to elucidate the primary effects fission cycling has on the r-process pattern. We also include fission-induced neutron emission when noted, implementing a piecewise linear fit of the values from Ref. [70]. We treat the emitted neutrons as becoming immediately thermalized with the surrounding medium.

As the fission material is reincorporated in the $A \approx 130$ peak, this material experiences "waiting points" and accumulates here as β decay is necessary for material to move from one isotopic (Z) chain to the next $(Z+1)$ chain. The material is initially compacted together in atomic mass space, A, and then disperses through β decay. Note that some material remains in each peak region during the fission cycling process as β decay does not fully deplete each peak.

To examine the accumulation of material during this β-decay dispersion process, we compare abundances in the second and third r-process peaks,

$$R_{\rm peak} = \frac{\sum_{A=190}^{200} Y(A)}{\sum_{A=125}^{135} Y(A)}. \quad (6)$$

Figure 1 demonstrates $R_{\rm peak}$ for a range of Y_e. The Y_e is from the start of of the r-process epoch. Each point represents an individual nucleosynthesis outcome resulting from a unique choice of electron neutrino and antineutrino luminosities in the neutrino-driven wind. The left-most portion ($Y_e \gtrsim 0.3$) of Fig. 1, where $R_{\rm peak}$ is zero, denotes where final r-process abundances extend from the second peak and up to the rare-earth region. The first bump, at $Y_e \approx 0.3$, denotes patterns where the heaviest r-process nuclides occupy the third peak and have partially left the second peak. Once past this bump, the heaviest r-process nuclides are beyond the third peak and have reached the fission region, and reincorporate into the second peak.

The behavior of fission under very neutron-rich conditions can be quantified by the number of fission cycles. When

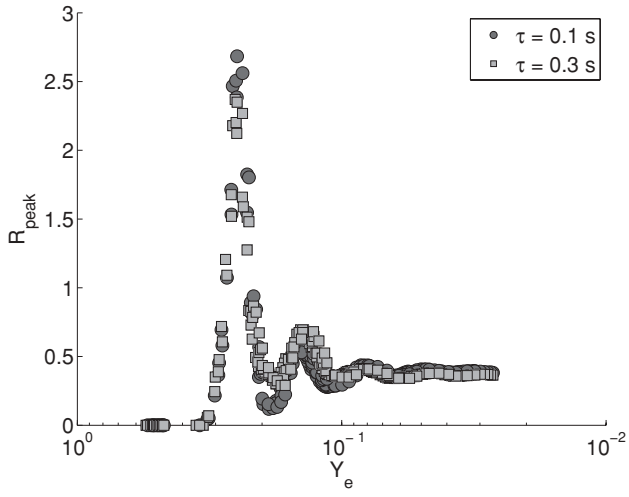

FIG. 1. The final $R_{\rm peak}$ [Eq. (6)] resulting from a symmetric fission distribution for two different outflow time scales, $\tau = 0.1$ s (circles) and $\tau = 0.3$ s (squares), is shown for a variety of electron fractions, Y_e. For very neutron-rich conditions, $Y_e \lesssim 0.1$, a consistent r-process pattern forms between the second, $A \approx 130$, and third, $A \approx 195$, peak region. Fission cycling during the r-process links the second and third peaks, as material that captures out of the third peak reaches the fission regime. The resulting fission daughter products then rejoin the r-process at the second peak.

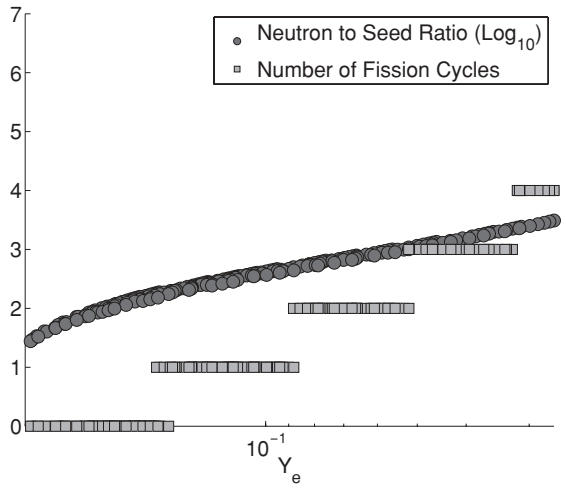

FIG. 2. The correspondence between Y_e and both the number of fission cycles, Eq. (7), and the neutron-to-seed ratio are shown for the conditions of Fig. 1 for our $\tau \approx 0.3$ s standard calculation. Each data point represents the outcome of an individual r-process calculation with different initial neutrino and antineutrino luminosities. The overlap in the number of fission cycles results from the influence of neutrinos on the abundance pattern as different sets of unique neutrino spectrum can result in similar electron fractions. Material begins to fission when $\gtrsim$200 free neutrons are present for each seed nuclei.

a nuclide fissions, there is an increase of heavy nuclei in abundance as multiple daughter nuclides are produced. The doubling of the total abundance is a fission cycle,

$$\Lambda = \log_2(Y_{\rm end}) - \log_2(Y_{\rm start}), \qquad (7)$$

where Λ is the number of fission cycles and $Y_{\rm start}$ and $Y_{\rm end}$ are the total abundance before and after fission cycling, respectively. The relationship between the electron fraction, Y_e, and both the number of fission cycles and neutron-to-seed ratio at the start of the r-process epoch is shown in Fig. 2 for our baseline calculation as described in Sec. I. The number of free neutrons per seed nuclei is influenced by the location of the fission termination point of the r process. For our standard calculation, we find fission cycling initially occurs for a neutron-to-seed ratio $\gtrsim 200$, consistent with previous studies, e.g., Ref. [71].

In Fig. 1, cycles occur at the minima past each bump and extend to the next minima. For example, the first fission cycle ranges from the minima at $Y_e \approx 0.17$ to the minima at $Y_e \approx 0.09$. Significant fission cycling occurs for increasingly neutron-rich conditions, and, under very neutron-rich conditions, the movement of material entering and leaving a peak reaches equilibrium, a consequence of steady β flow.

The equilibrium $R_{\rm peak}$, due to fission cycling, appears as the straight region of the curve in Fig. 1 for $Y_e \lesssim 0.1$ and does not change significantly for variations in the wind conditions. This is depicted in Fig. 1 as the equilibrium peak ratio is not strongly affected by choice of the outflow time scale. Here, this stability is demonstrated for the wind outflow time scales of $\tau = 0.1$ s and $\tau = 0.3$ s.

The equilibrium value of $R_{\rm peak}$ is sensitive to properties of the fission model. In particular, it is sensitive to the specific location within the second peak to which fission returns material, as the presence of waiting points here dictate the flow and accumulation of material. Material deposited at or below closed-shell nuclei flow to a waiting point and remain in this peak region longer than material deposited above the closed-shell nuclei. The accumulation of material in the $A \approx 130$ peak leads to smaller values of $R_{\rm peak}$. Material arriving above the closed shell bypasses the waiting point and continues flowing to heavier regions, leading to larger values of $R_{\rm peak}$.

In Fig. 3 we show specific examples of the consequences to $R_{\rm peak}$ resulting from different fission daughter product distributions. We consider cases of fission daughter product distributions with both symmetric and asymmetric modes. Symmetric distributions have daughter nuclides that are close in both charge, Z, and mass, A. These distributions deposit more material at or below the closed-shell nuclides and have a smaller equilibrium $R_{\rm peak}$, shown as circles in Fig. 3. Asymmetric distributions have daughter product distributions whose charge and mass are separated proportionally by a scaling factor, resulting in one daughter being larger in both A and Z than the other. This leads to more material being deposited above the closed-shell nuclides and a higher equilibrium $R_{\rm peak}$, shown as diamonds in Fig. 3. When neutrons are emitted during the course of fission, fewer daughter products lie above the close-shell nuclei, lowering the equilibrium $R_{\rm peak}$ from the asymmetric case, shown as squares in Fig. 3.

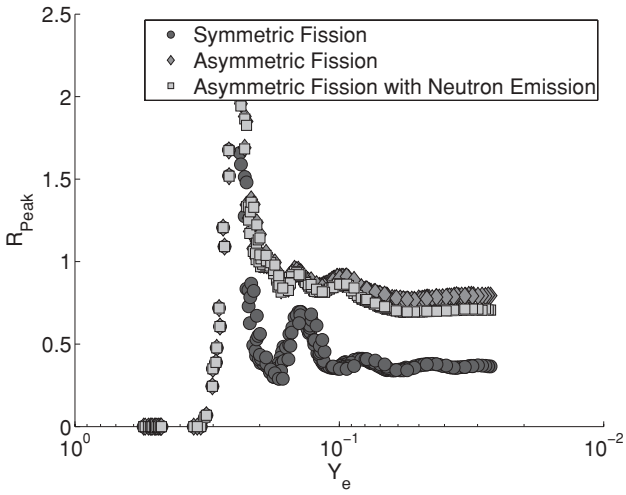

FIG. 3. Same as Fig. 1 but comparing the effects of different fission daughter product distributions. The distribution of daughter products determines if material is deposited above or below the closed-shell nuclei in the $A \approx 130$ peak. Fission distributions depositing material above the closed-shell nuclides, asymmetric fission (diamonds), leads to a higher equilibrium $R_{\rm peak}$, as more material is cycled through the $A \approx 130$ peak. Distributions depositing material below the peak, symmetric fission (circles), have a lower equilibrium $R_{\rm peak}$ and cycle less material through the peak region. Fission-induced neutron emission deposits additional material below the closed-shell nuclides, lowering $R_{\rm peak}$, and is shown above for asymmetric fission (squares).

Detailed knowledge of both the fission location and daughter product distributions is required to fully model the r-process abundances in very neutron-rich environments.

The change in abundance of the various r-process peaks during fission cycling, as depicted in Figs. 1 and 3, can be phenomenologically described by the effective rate of material entering and exiting the major peak regions. The effect of fission cycling on the peak abundances is modeled by approximating the flow of fission material as rapid compared to the flow leaving the $A \approx 130$, the rare-earth, and the $A \approx 195$ peak regions. The rate of abundance change in each peak becomes:

$$\dot{Y}_{130} = -\Gamma_{130}(t)Y_{130} + f\Gamma_{195}(t)Y_{195} \quad (8)$$

$$\dot{Y}_{\text{Earth}} = -\Gamma_{\text{Earth}}(t)Y_{\text{Earth}} + \Gamma_{130}(t)Y_{130} + (2-f)\Gamma_{195}(t)Y_{195} \quad (9)$$

$$\dot{Y}_{195} = -\Gamma_{195}(t)Y_{195} + \Gamma_{\text{Earth}}(t)Y_{\text{Earth}}, \quad (10)$$

where Y is the abundance of each peak and Γ is the rate of decay leaving a region, with the subscripts corresponding to the $A \approx 130$, rare-earth, and $A \approx 195$ peaks. Here f is the distribution of fission daughter products between the $A \approx 130$ and rare-earth regions. For purposes of illustrating the toy model, we take all fission products as arriving to the $A \approx 130$ region, $f = 2$. The equilibrium (steady β flow) behavior of fission cycling is depicted in the far right-hand region of Fig. 1. For discussion of solutions for long-time fission cycling, see Ref. [51]. The transient region prior to steady β-flow equilibrium is dependent on the flow (decay rate) of material leaving each peak region, Γ_{130}, Γ_{Earth}, and Γ_{195}. The effective flow out of a region is determined by the β-decay rate of each isotopic chain, as material is in $(n,\gamma) \leftrightharpoons (\gamma,n)$ equilibrium during this fission cycling phase. Additionally, this outflow is determined by the population of nuclides within a peak, because the individual β-decay rate changes from nuclide to nuclide. As a consequence, various nuclides are populated while material is flowing through each peak, leading to changes in the effective flow out of each peak. For example, the effective flow rate in the $A \approx 130$ peak slows as the closed-shell nuclides, with slow β-decay rates, are populated. We employ our phenomenological model to highlight the change in the effective flow rate in Fig. 4, for the $A \approx 130$ peak region with a $Y_e = 0.05$ at the start of the r process. Here, the fluctuation in the decay rates of a peak corresponds to the changing of individual nuclide abundances. The movement of material within a peak is demonstrated by the corresponding change of the weighted atomic number, Z. As the conditions in Fig. 4 are very neutron rich, sufficient for steady β flow, the right-most portion depicts a straight line for both the effective flow rate and Z, because steady β flow leads to isotopic chain abundances determined by the β-decay rate of each chain.

IV. STEADY β FLOW

As discussed in Sec. I, the abundances of the r process become fully determined under conditions where both fission cycling and steady β flow occur. We now examine consequences to the final r-process abundances resulting from

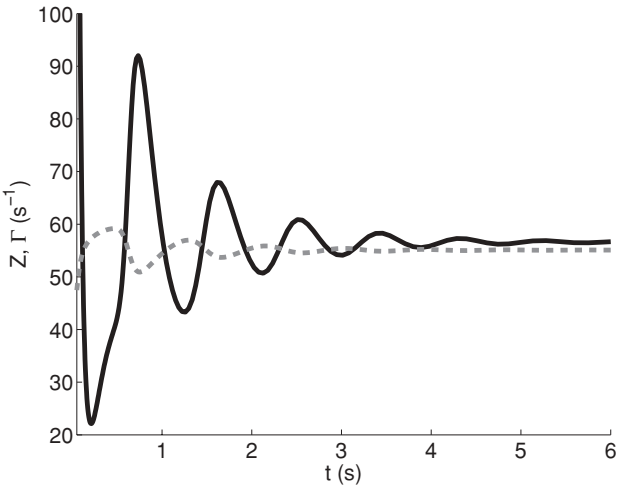

FIG. 4. Under very neutron-rich conditions the effective decay rate of the peaks oscillate until equilibrating at the steady β-flow rate. The abundance weighted atomic number, $Z = \sum_{Z=45}^{60} ZY(Z) / \sum_{Z=45}^{60} Y(Z)$, (dashes) is plotted with the abundance weighted β-decay rate, $\Gamma = \sum_{Z=45}^{60} \Gamma_\beta(Z)Y(Z) / \sum_{Z=45}^{60} Y(Z)$, of an isotopic chain (solid) for the second, $A \approx 130$, peak region, versus time, t. The oscillation of the decay rates in the peak regions are due to the changing population of different nuclides during the course of fission cycling. To elucidate abundance changes between isotopic chains, the data above results from our phenomenological model, Eq. (8), under conditions with an $Y_e = 0.05$ at the start of the r-process epoch ($T_9 \approx 2.5$).

steady β flow. In Fig. 5, the steady-β flow condition, Eq. (5), is tested and fulfilled for very neutron-rich conditions in the neutrino-driven wind, appearing as a straight line between the

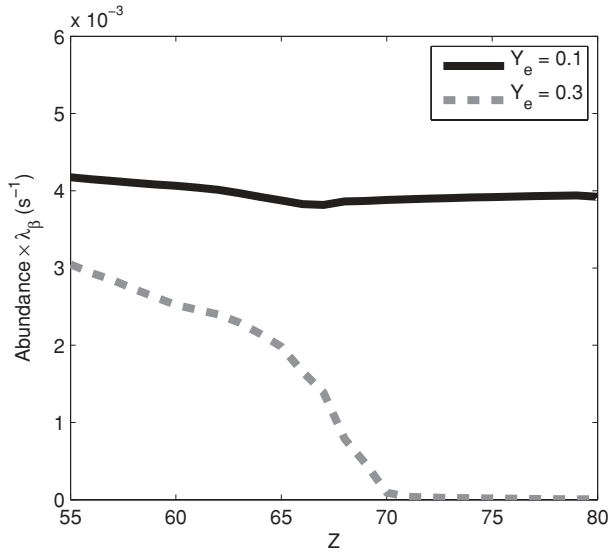

FIG. 5. We plot the steady β-flow condition, $\sum_A Y(Z,A)\lambda_\beta(Z,A)$, versus atomic number, Z, for two different Y_e's in the neutrino-driven wind. For the case with an $Y_e = 0.1$ at the start of the r-process epoch, conditions are sufficiently neutron rich for steady β flow, marked by a straight line. The case with $Y_e = 0.3$ is not neutron rich enough for steady β flow to obtain.

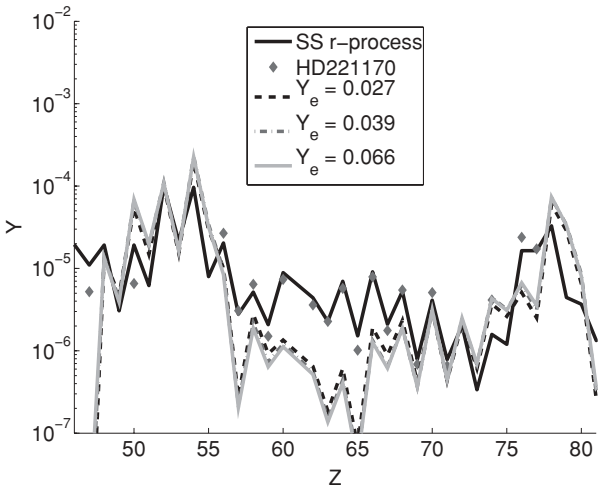

FIG. 6. When conditions neutron rich enough for steady β flow occur, a consistent r-process pattern emerges regardless of the initial Y_e. The details of the abundance pattern are dependent on the nuclear physics employed in the mass model, as discussed in the text. The abundance, Y, is plotted versus the atomic number, Z, for these very neutron-rich conditions. The dashed line is generated in the neutrino-driven wind for $L_{\nu_e} = 0.02$ and $L_{\bar{\nu}_e} = 3.0$, the dashed-dotted line for $L_{\nu_e} = 0.01$ and $L_{\bar{\nu}_e} = 4.0$, and the solid line for $L_{\nu_e} = 0.006$ and $L_{\bar{\nu}_e} = 6.0$. The electron neutrino and antineutrino luminosities, L_{ν_e} and $L_{\bar{\nu}_e}$, are in units of $\times 10^{51}$ ergs s^{-1}. The effective temperature of the electron neutrinos is $T_{\nu_e} = 3.5$ MeV and for the electron antineutrinos is $T_{\bar{\nu}_e} = 4.5$ MeV. Labeled is Y_e at the start of the r-process epoch. The black line represents the solar system abundances from [77], and the gray diamonds are the r-process abundances from the halo star HD 221170 [78]. All abundances are scaled to 10^{-4} at $Z = 52$.

second and third peaks of the r process, the main r-process region. For less neutron-rich conditions, steady β flow does not obtain as there are not enough free neutrons to sustain repopulation of the seed nuclei by fission cycling.

A set of typical abundances resulting from steady β flow, occurring for very neutron-rich conditions in the neutrino-driven wind, are depicted in Fig. 6. The individual Y_e's are produced by a unique choice of initial neutrino and antineutrino luminosities, in the same manner as Fig. 1. Our abundance patterns reproduce the general peak structure of the main r process between the second and third peaks and is robust over a wide range of conditions in the neutrino-driven wind, directly resulting from the pairing of both fission cycling and steady β flow. Improvement to a nuclide by nuclide abundance comparison between calculation and both solar and halo star abundance data requires further understanding of the nuclear properties of nuclei far from stability and processes that influence the abundance pattern after freeze-out [72–74].

Abundance yields resulting from the joint operation of both fission cycling and steady β flow produce a consistent pattern of r-process abundances that extends to elements in the actinide region. The main r process does not appear to extend past $Z > 82$, however. It is possible that the abundance of elements in the actinide region relative to those between the second and third r-process region can be influenced by mechanisms external to the formation of the r process by both fission cycling and steady β flow, allowing the final abundances of these elements to emerge independently from the consistent pattern of r-process elements between the second and third peak region. These mechanisms may include post-freeze-out neutrino-induced fission [74] and contributions from an r process that yields elements only near the actinide region [75]. Additional discussion on the abundance of the r-process elements in the actinide region may be found in Goriely and Arnould 2001 [75].

It has previously been shown, e.g., Ref. [76], that consistent patterns of r-process elements form in the rare-earth region, between $60 \lesssim Z \lesssim 70$, due to the absence of waiting point nuclei in this region. Under particular wind conditions, $\tau = 0.005$ s, for example, the resulting r-process abundance pattern can reproduce the full, observed region of consistent r-process elements, $56 \lesssim Z < 76$ [18], as found in the halo star data. In contrast, our calculations demonstrate that when steady β flow is jointly accompanied by fission cycling, the region of universality is not dependent on the wind conditions and extends between the fission daughter products and the fission termination point of the r process.

V. INFLUENCE OF NEUTRINOS ON THE ELECTRON FRACTION

After neutrinos extricate material from the surface of the proto-neutron star, the newly released material is composed entirely of free nucleons. Although we dynamically calculate the Y_e in our models, it is pedagogically useful to examine the electron fraction through the approximation of weak equilibrium. Because neutrino and antineutrino rates dominate electron and positron capture, the initial weak equilibrium $Y_e^{(0)}$ is

$$Y_e^{(0)} \approx \frac{1}{1 + \lambda_{\bar{\nu}_e}/\lambda_{\nu_e}}. \tag{11}$$

The rates of electron neutrino capture on neutrons and electron antineutrino capture on protons are λ_{ν_e} and $\lambda_{\bar{\nu}_e}$, respectively. An increase in the electron antineutrino capture rate, achievable by either boosting the electron antineutrino flux or hardening the electron antineutrino spectra, will tend to decrease Ye, whereas an increase in the neutrino capture rate will tend to increase Ye.

Farther away from the proto-neutron star, as material in the expansion continues to cool, α particles form and contribute to the weak equilibrium Y_e approximation,

$$Y_e \approx Y_e^{(0)} + \left[\tfrac{1}{2} - Y_e^{(0)}\right] X_\alpha. \tag{12}$$

Here, X_α represents the mass fraction of α particles.

The formation of α particles is enhanced in the presence of a strong electron neutrino flux, as electron neutrinos capturing on free neutrons create new effective proton seeds for α-particle formation. These effective seeds quickly capture additional neutrons which continues to drive the Y_e to 1/2. The depletion of neutrons from both neutrino capture and α-particle formation is known as the alpha effect, and this alpha effect

must be removed for neutron-rich conditions to obtain for the r process.

We look to neutrino luminosities and spectral properties for the removal of the alpha effect. Because weak equilibrium does not fully obtain in the neutrino-driven wind, we use the following procedure to calculate Y_e instead of the weak equilibrium approximation described above. Starting from a prospective set of neutrino effective temperatures and luminosities, we adjust the initial Fermi-Dirac neutrino spectrum. Then we self-consistently account for both the evolution of the updated neutrino spectrum in the neutrino-driven wind and the relevant changes to the abundance. From this, we dynamically account for the Y_e throughout the nucleosynthesis epochs. For a full description, see Ref. [50].

We first examine Y_e's resulting from a range of neutrino effective temperatures. Before the formation of α particles, $T_9 \approx 9.4$, the Y_e's from our model are consistent with weak equilibrium. The Y_e increases with larger electron neutrino effective temperatures as these higher temperatures result in more protons being converted to neutrons. This results from electron neutrino capture on neutrons, Eq. (1). Conversely, larger antineutrino energies produce a lower Y_e, a consequence of electron anti-neutrino capture, Eq. (2). The ranges of neutrino effective temperatures depicted in the left panel of Fig. 7 result in Y_e between $0.1 \lesssim Y_e \lesssim 0.6$, and the low Y_e portion of the region seems initially promising for a successful r process. In Fig. 7, the luminosity of the electron neutrinos is 1×10^{51} ergs s^{-1} and the electron antineutrino luminosity is 1.3×10^{51} ergs s^{-1}.

After α-particle formation and charged particle reactions have occurred, conditions generated by changes to the neutrino effective temperatures do not lead to a successful r process. The Y_e at the r-process epoch is shown in the right panel of Fig. 7 and is noticeably compressed by the alpha effect, ranging between $0.4 \lesssim Y_e \lesssim 0.5$. The Y_e is increased compared to the previous epoch as the alpha effect has converted free neutrons into additional effective proton seed nuclei. These values of Y_e are not neutron rich enough to lead to a successful r process.

The second case we examine is for changes in the neutrino and antineutrino luminosities. Although initially similar, they lead to a decidedly different outcome, as environments where sufficient reductions in the electron neutrino luminosity occur can lead to a successful r process. When both the neutrino and antineutrino luminosities are significantly reduced compared to traditional models, electron capture and positron capture become important and influence the electron fraction,

$$Y_e \approx 1/\left[1 + \left(\lambda_{\bar{\nu}_e} + \lambda_{e^-}\right)/\left(\lambda_{\nu_e} + \lambda_{e^+}\right)\right], \tag{13}$$

where λ_{e^-} and λ_{e^+} are the electron and positron rates, respectively [45]. When electron-positron pairs are important, as they are here, these rates tend to increase the Y_e and begin influencing the Y_e when the neutrino luminosities are $L_{\nu_e} \lesssim 10^{50}$ ergs s^{-1} and $L_{\bar{\nu}_e} \lesssim 5 \times 10^{50}$ ergs s^{-1}. For wind solutions where neutrinos are less prevalent, a weak equilibrium Y_e dictated by electron and positron capture would not be sufficiently neutron rich for the r process.

For reductions in the electron neutrino luminosity relative to the traditional wind model, but not in the electron antineutrino luminosity, a very large variety of Y_e's result, $0.1 \lesssim Y_e \lesssim 0.8$, as shown in the left panel of Fig. 8. Similar to the case with effective neutrino temperatures, lowering the electron neutrino luminosities, L_{ν_e}, decreases the Y_e and leads to neutron-rich conditions. These early Y_e's from the changed rates in Eq. (1) and Eq. (2) are again consistent with the weak equilibrium values. For all of Fig. 8, we take the effective electron neutrino temperature to be $T_{\nu_e} = 3.5$ MeV and the electron antineutrino temperature as $T_{\bar{\nu}_e} = 4.5$ MeV.

Near the r-process epoch, $T_9 \approx 2.5$, changes to the neutrino luminosities continue to produce a large spread of Y_e's, as depicted in the right panel of Fig. 8. A successful r process can occur for reductions to the electron neutrino luminosity of $L_{\nu_e} \lesssim 2.3 \times 10^{50}$ ergs s^{-1}. For these decreased electron neutrino luminosities, the depletion of free neutrons by the

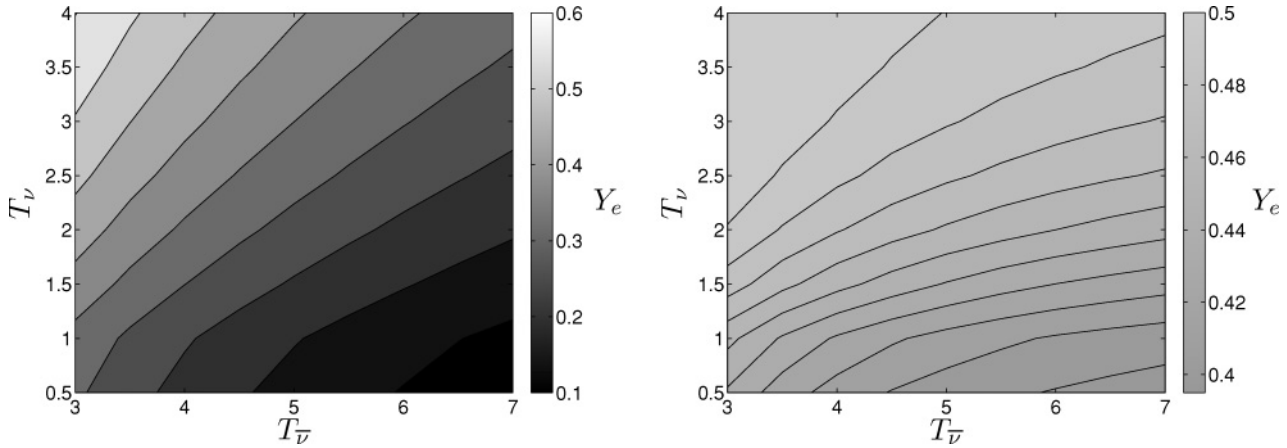

FIG. 7. The electron fraction, Y_e, is shown over a range of electron neutrino and antineutrino temperatures, T_ν and $T_{\bar{\nu}}$. The "alpha" effect equally binds protons and neutrons into α particles, which drives the electron fraction to $Y_e \approx 1/2$ and prevents an r process. Regions of Y_e before α-particle formation ($T_9 \approx 9.4$; left panel) initially appear favorable to the r process; however, the "alpha" effect has pushed Y_e near $1/2$ by the start of the r-process epoch ($T_9 \approx 2.5$; right panel). The effective electron neutrino and antineutrino temperatures, T_ν and $T_{\bar{\nu}}$, are in units of MeV. The electron neutrino luminosity is $L_\nu = 1 \times 10^{51}$ ergs s^{-1} and the electron antineutrino luminosity is $L_{\bar{\nu}} = 1.3 \times 10^{51}$ ergs s^{-1}.

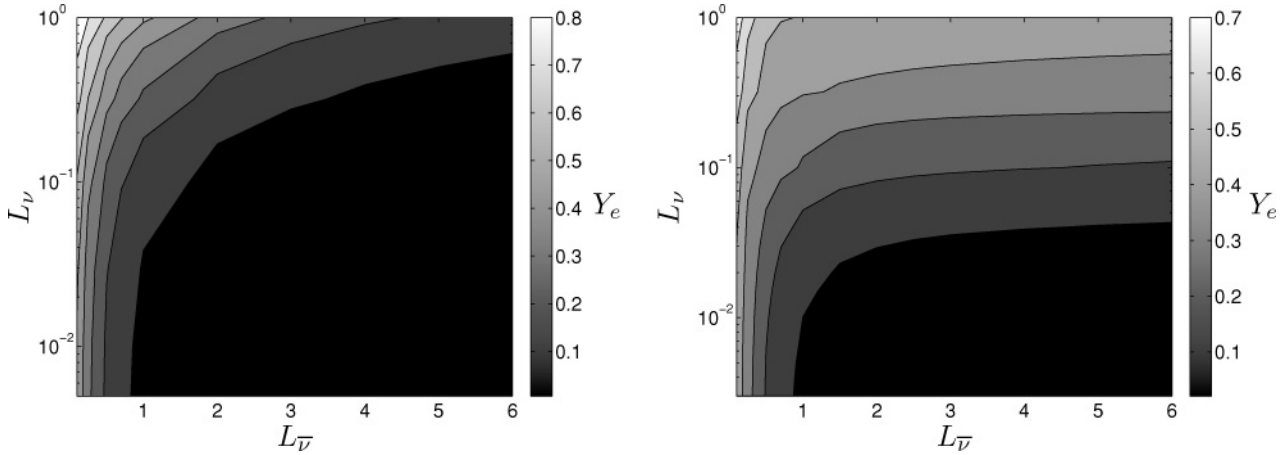

FIG. 8. The electron fraction, Y_e, is shown over a range of electron neutrino and antineutrino luminosities, L_ν and $L_{\overline{\nu}}$. A reduction in the electron neutrino luminosity, L_ν, prevents the "alpha" effect and leads to a successful r process. The "alpha" effect is avoided as reducing the electron neutrino luminosity, L_ν, lowers the rate of neutrino capture on neutrons forming protons, Eq. (1). The electron fraction, Y_e, is favorable for the r process before α-particle formation ($T_9 \approx 9.4$; left panel) and reductions in L_ν lead to a low Y_e conditions for the r process (right panel). The electron neutrino and antineutrino luminosities, L_ν and $L_{\overline{\nu}}$, are in units of $\times 10^{51}$ ergs s^{-1}. The effective temperature of the electron neutrinos is $T_\nu = 3.5$ MeV and for the electron antineutrinos is $T_{\overline{\nu}} = 4.5$ MeV. For low values of both L_ν and $L_{\overline{\nu}}$, electron and positron capture set the Y_e.

alpha effect is diminished as fewer new protons are made available through Eq. (1). The neutrino luminosities that lead to a successful r process are shown by all three shaded regions in Fig. 9.

We note that neutron-rich conditions beyond the minimum required to produce an r process occur in our study of the neutrino luminosities. In fact, order of magnitude reductions of L_{ν_e} lead to conditions where fission cycling can occur in the r process. For a $\tau = 0.3$ s wind time scale, $Y_e \lesssim 0.17$ are sufficient to lead to fission cycling, depicted in the medium gray and black regions of Fig. 9. Conditions even more neutron-rich, $Y_e \lesssim 0.1$, lead to a steady flow solution within fission cycling, as described in Sec. IV, reproducing the general features of the halo star data and providing an intriguing solution for the realization of a main r process. This scenario is shown in Fig. 9 as the black region. The necessary large reductions to the L_{ν_e} could be a consequence of either active-sterile neutrino oscillations [50] or other new physics.

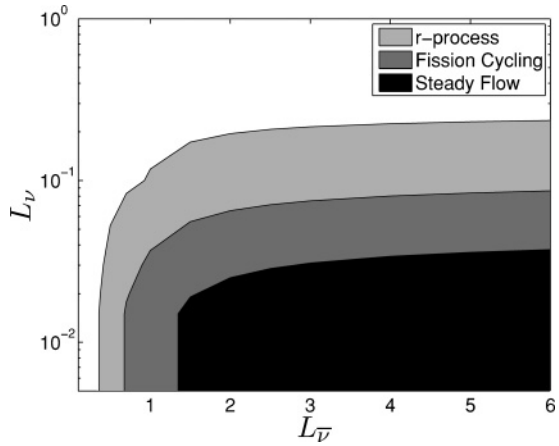

FIG. 9. Under the wind conditions of Fig. 8, neutrino luminosities, L_ν and $L_{\overline{\nu}}$ in units of $\times 10^{51}$ ergs s^{-1}, necessary for a successful r process (all shaded regions), the presence of fission cycling (medium gray and black), and for the presence of steady β flow (black) are shown.

VI. CONCLUSIONS

In the neutrino-driven wind, fission cycling during r-process nucleosynthesis occurs for low electron fractions and, when combined with steady β flow, reproduces the basic features of the main r process. During fission cycling, material effectively captures out of the third peak and returns to the second peak by fission processes, linking the second and third peaks and creating a main r process. For $0.1 \lesssim Y_e \lesssim 0.3$, these abundance patterns retain some dependence on the initial Y_e.

At even lower electron fractions, $Y_e \lesssim 0.1$, steady β flow occurs during the r process and the abundance patterns produced are consistent over small changes to the astrophysical conditions. Steady β flow is a consequence of the presence of both fission cycling and $(n,\gamma) \rightleftharpoons (\gamma,n)$ equilibrium. Fission cycling creates seed nuclei at the second peak, and $(n,\gamma) \rightleftharpoons (\gamma,n)$ equilibrium determines the r-process path. After $(n,\gamma) \rightleftharpoons (\gamma,n)$ equilibrium fixes the path, β decay between the isotopic chains equilibrate as the first and last chains are connected by fission. This produces an abundance pattern that is not sensitive to the exact initial Y_e. The steady β-flow abundances strongly depend on the details of fission.

As the final r-process abundance pattern is very sensitive to the details of fission, see Fig. 3, it is paramount to improve our understanding of which heavy nuclides participate in fission during the r process and to develop a more precise determination of the daughter products that result. The presence of fission in the r process may provide a termination point for the r process, furthering the understanding of

which heavy nuclides play a role in the r process. Under neutron-rich conditions, the distribution of fission daughter products influences the shape of the r process. If the r process occurs in very neutron-rich environments, the fission daughter product distribution also determines the starting isotopic chain of steady β flow, impacting the region where steady β flow abundances form and may be important to the understanding of the formation of a main r process.

Low Y_e's at the r-process epoch are not found in the traditional neutrino-driven wind. Before the onset of α-particle formation, a large range of electron neutrino and antineutrino effective temperatures and luminosities would yield low-Y_e environments. The electron fraction is driven to $Y_e \approx 1/2$ as α-particle formation binds protons and neutrons in equal numbers. Changes to the effective temperatures in the ranges of $0.5\ \text{MeV} < T_\nu < 4\ \text{MeV}$ for electron neutrinos and $3\ \text{MeV} < T_{\overline{\nu}} < 7\ \text{MeV}$ for electron antineutrinos result in environments with an "alpha" effect and do not yield a main r process. Given the physics discussed in this article, realization of the main r process in a conventional neutrino-driven wind is a challenge. However, it can occur with a reduction in the electron neutrino capture rate while the electron antineutrino capture rate remains unchanged. Future studies on the details of neutrinos, particularly in the postcore bounce supernova environment, as well as physics beyond the standard model, would benefit the understanding of an r process in the neutrino-driven wind.

ACKNOWLEDGMENTS

This work was partially supported by the Department of Energy under contracts DE-FG05-05ER41398 (R.S.) and DE-FG02-02ER41216 (G.C.M.). This work was partially supported by the United States National Science Foundation under contract PHY-0244783 (W.R.H.). Oak Ridge National Laboratory (W.R.H.) is managed by UT-Battelle, LLC, for the U.S. Department of Energy under contract DE-AC05-000R22725. We acknowledge useful discussions with Gabriel Martinez-Pindedo and Fredrich-Karl Thielemann.

[1] E. M. Burbidge, G. R. Burbidge, W. A. Fowler, and F. Hoyle, Rev. Mod. Phys. **29**, 547 (1957).
[2] A. G. W. Cameron, Pub. Astron. Soc. Pac. **69**, 201 (1957).
[3] B. S. Meyer, Annu. Rev. Astron. Astrophys. **32**, 153 (1994).
[4] A. McWilliam, G. W. Preston, C. Sneden, and L. Searle, Astron. J. **109**, 2757 (1995).
[5] C. Sneden, A. McWilliam, G. W. Preston, J. J. Cowan, D. L. Burris, and B. J. Armosky, Astrophys. J. **467**, 819 (1996).
[6] A. McWilliam, Astron. J. **115**, 1640 (1998).
[7] D. L. Burris, C. A. Pilachowski, T. E. Armandroff, C. Sneden, J. J. Cowan, and H. Roe, Astrophys. J. **544**, 302 (2000).
[8] J. Westin, C. Sneden, B. Gustafsson, and J. J. Cowan, Astrophys. J. **530**, 783 (2000).
[9] R. Cayrel, V. Hill, T. C. Beers, B. Barbuy, M. Spite, F. Spite, B. Plez, J. Andersen, P. Bonifacio, and P. François *et al.*, Nature **409**, 691 (2001).
[10] V. Hill, B. Plez, R. Cayrel, T. C. Beers, B. Nordström, J. Andersen, M. Spite, F. Spite, B. Barbuy, P. Bonifacio *et al.*, Astron. Astrophys. **387**, 560 (2002).
[11] J. J. Cowan, C. Sneden, S. Burles, I. I. Ivans, T. C. Beers, J. W. Truran, J. E. Lawler, F. Primas, G. M. Fuller, B. Pfeiffer *et al.*, Astrophys. J. **572**, 861 (2002).
[12] C. Sneden, J. J. Cowan, J. E. Lawler, I. I. Ivans, S. Burles, T. C. Beers, F. Primas, V. Hill, J. W. Truran, G. M. Fuller *et al.*, Astrophys. J. **591**, 936 (2003).
[13] S. Honda, W. Aoki, T. Kajino, H. Ando, T. C. Beers, H. Izumiura, K. Sadakane, and M. Takada-Hidai, Astrophys. J. **607**, 474 (2004).
[14] N. Christlieb, T. C. Beers, P. S. Barklem, M. Bessell, V. Hill, J. Holmberg, A. J. Korn, B. Marsteller, L. Mashonkina, Y.-Z. Qian *et al.*, Astron. Astrophys. **428**, 1027 (2004).
[15] A. Frebel, N. Christlieb, J. E. Norris, C. Thom, T. C. Beers, and J. Rhee, Astrophys. J. Lett. **660**, L117 (2007).
[16] F. Montes, T. C. Beers, J. Cowan, T. Elliot, K. Farouqi, R. Gallino, M. Heil, K.-L. Kratz, B. Pfeiffer, M. Pignatari *et al.*, ApJ **671**, 1685 (2007).
[17] J. J. Cowan, C. Sneden, J. E. Lawler, and E. A. D. Hartog, PoS **NIC-IX**, 014 (2006).
[18] M. Arnould, S. Goriely, and K. Takahashi, Phys. Rep. **450**, 97 (2007).
[19] J. Beun, G. C. McLaughlin, R. Surman, and W. R. Hix, PoS **NIC-IX**, 140 (2006).
[20] G. Martínez-Pinedo, A. Kelic, K. Langanke, K. Schmitt, D. Mocelj, C. Fröhlich, F. K. Thielemann, I. Panov, T. Rauscher, M. Liebendörfer, N. T. Zinner, B. Pfeiffer, R. Buras, and H. Janka, PoS **NIC-IX**, 064 (2006).
[21] B. S. Meyer, Astrophys. J. **343**, 254 (1989).
[22] B. S. Meyer, G. J. Mathews, W. M. Howard, S. E. Woosley, and R. D. Hoffman, Astrophys. J. **399**, 656 (1992).
[23] S. E. Woosley, J. R. Wilson, G. J. Mathews, R. D. Hoffman, and B. S. Meyer, Astrophys. J. **433**, 229 (1994).
[24] F. K. Thielemann *et al.*, Prog. Part. Nucl. Phys. **46**, 5 (2001).
[25] S. Rosswog, E. Ramirez-Ruiz, and M. B. Davies, MNRAS **345**, 1077 (2003).
[26] S. Goriely, P. Demetriou, H.-T. Janka, J. M. Pearson, and M. Samyn, Nucl. Phys. **A758**, 587 (2005).
[27] S. Wanajo, T. Kajino, G. J. Mathews, and K. Otsuki, Astrophys. J. **554**, 578 (2001).
[28] D. Argast, M. Samland, F. K. Thielemann, and Y. Z. Qian, Astron. Astrophys. **416**, 997 (2004).
[29] R. D. Hoffman, S. E. Woosley, and Y.-Z. Qian, Astrophys. J. **482**, 951 (1997).
[30] T. A. Thompson, A. Burrows, and B. S. Meyer, Astrophys. J. **562**, 887 (2001).
[31] Y.-Z. Qian, Prog. Part. Nucl. Phys. **50**, 153 (2003).
[32] Y.-Z. Qian and S. E. Woosley, Astrophys. J. **471**, 331 (1996).
[33] C. Y. Cardall and G. M. Fuller, Astrophys. J. Lett. **486** L111+ (1997).
[34] K. Otsuki, H. Tagoshi, T. Kajino, and S.-Y. Wanajo, Astrophys. J. **533**, 424 (2000).
[35] K. Sumiyoshi, M. Terasawa, G. J. Mathews, T. Kajino, S. Yamada, and H. Suzuki, Astrophys. J. **562**, 880 (2001).

[36] S. Wanajo, M. Tamamura, N. Itoh, K. Nomoto, Y. Ishimaru, T. C. Beers, and S. Nozawa, Astrophys. J. **593**, 968 (2003).
[37] S. W. Bruenn, Astrophys. J. **340**, 955 (1989).
[38] S. W. Bruenn, Astrophys. J. **341**, 385 (1989).
[39] A. Arcones, H.-T. Janka, and L. Scheck, A & A **467**, 1227 (2007).
[40] S. Wanajo, ApJ **666**, L77 (2007).
[41] A. Burrows, L. Dessart, E. Livne, C. D. Ott, and J. Murphy, ApJ **664**, 416 (2007).
[42] B. D. Metzger, T. A. Thompson, and E. Quataert, Astrophys. J. **659**, 561 (2007).
[43] R. Surman and G. C. McLaughlin, Astrophys. J. **603**, 611 (2004).
[44] R. Surman, G. C. McLaughlin, and W. R. Hix, Astrophys. J. **643**, 1057 (2006).
[45] G. C. McLaughlin, G. M. Fuller, and J. R. Wilson, Astrophys. J. **472**, 440 (1996).
[46] G. M. Fuller and B. S. Meyer, Astrophys. J. **453**, 792 (1995).
[47] B. S. Meyer, G. C. McLaughlin, and G. M. Fuller, Phys. Rev. C **58**, 3696 (1998).
[48] G. C. McLaughlin, J. M. Fetter, A. B. Balantekin, and G. M. Fuller, Phys. Rev. C **59**, 2873 (1999).
[49] J. Fetter, G. C. McLaughlin, A. B. Balantekin, and G. M. Fuller, Astropart. Phys. **18**, 433 (2003).
[50] J. Beun, G. C. McLaughlin, R. Surman, and W. R. Hix, Phys. Rev. D **73**, 093007 (2006).
[51] P. A. Seeger, W. A. Fowler, and D. D. Clayton, ApJS **11**, 121 (1965).
[52] I. V. Panov, E. Kolbe, B. Pfeiffer, T. Rauscher, K.-L. Kratz, and F.-K. Thielemann, Nucl. Phys. **A747**, 633 (2005).
[53] J. J. Cowan, F.-K. Thielemann, and J. W. Truran, Phys. Rep. **208**, 267 (1991).
[54] R. C. Duncan, S. L. Shapiro, and I. Wasserman, Astrophys. J. **309**, 141 (1986).
[55] C. L. Fryer, F. Herwig, A. Hungerford, and F. X. Timmes, Astrophys. J. Lett. **646**, L131 (2006).
[56] W. R. Hix and F. K. Thielemann, J. Comp. App. Math. **109**, 321 (1999).
[57] T. Rauscher and F.-K. Thielemann, At. Data Nucl. Data Tables **75**, 1 (2000).
[58] G. C. McLaughlin and G. M. Fuller, Astrophys. J. **455**, 202 (1995).
[59] R. Surman and J. Engel, Phys. Rev. C **64**, 035801 (2001).
[60] R. Surman, J. Engel, J. R. Bennett, and B. S. Meyer, Phys. Rev. Lett. **79**, 1809 (1997).
[61] P. Möller, J. R. Nix, and K.-L. Kratz, At. Data Nucl. Data Tables **66**, 131 (1997).
[62] J. J. Cowan, F.-K. Thielemann, and J. W. Truran, Astrophys. J. **323**, 543 (1987).
[63] T. Rauscher, J. H. Applegate, J. J. Cowan, F.-K. Thielemann, and M. Wiescher, Astrophys. J. **429**, 499 (1994).
[64] J. J. Cowan, B. Pfeiffer, K.-L. Kratz, F.-K. Thielemann, C. Sneden, S. Burles, D. Tytler, and T. C. Beers, Astrophys. J. **521**, 194 (1999).
[65] C. Freiburghaus, J.-F. Rembges, T. Rauscher, E. Kolbe, F.-K. Thielemann, K.-L. Kratz, B. Pfeiffer, and J. J. Cowan, Astrophys. J. **516**, 381 (1999).
[66] E. R. Hilf *et al*., Suppl. to Proc. Int. Conf. NFFS-3 **76-13**, 142 (1976).
[67] I. V. Panov and F.-K. Thielemann, Astronomy Letters **30**, 647 (2004).
[68] E. Kolbe, K. Langanke, and G. M. Fuller, Phys. Rev. Lett. **92**, 111101 (2004).
[69] M. Terasawa, K. Langanke, T. Kajino, G. J. Mathews, and E. Kolbe, Astrophys. J. **608**, 470 (2004).
[70] A. Kelić, N. Zinner, E. Kolbe, K. Langanke, and K.-H. Schmidt, Phys. Lett. **B616**, 48 (2005).
[71] B. S. Meyer and J. S. Brown, ApJS **112**, 199 (1997).
[72] J. M. Pearson, R. C. Nayak, and S. Goriely, Phys. Lett. **B387**, 455 (1996).
[73] J. Duflo and A. P. Zuker, Phys. Rev. C **52**, R23 (1995).
[74] Y. Z. Qian, Astrophys. J. **569**, L103 (2002).
[75] S. Goriely and M. Arnould, Astronomy and Astrophysics **379**, 1113 (2001).
[76] K. Otsuki, G. J. Mathews, and T. Kajino, New Astron. **8**, 767 (2003).
[77] J. Simmerer *et al*., Astrophys. J. **617**, 1091 (2004).
[78] I. I. Ivans, J. Simmerer, C. Sneden, J. E. Lawler, J. J. Cowan, R. Gallino, and S. Bisterzo, Astrophys. J. **645**, 613 (2006).